

Modeling and reactive navigation of an autonomous sailboat

Clément Pêtrès, Miguel-Angel Romero-Ramirez, Frédéric Plumet and Bertrand Alessandrini

Abstract—Among Autonomous Surface Vehicles (ASV), sailboat robots could be an efficient solution for long term missions and semi-persistent presence in the oceans since they rely on renewable energy like solar and wind energies. However, steering of such vehicles presents an inherent difficulty since the thrust force heavily rely on the wind (speed and direction) and sail angle as well as on the underlying complex dynamic properties of the ship, mainly due to the aero and hydrodynamic forces. This paper proposes a new reactive path planning method which takes into account the so called no-go zones and turns them into virtual obstacles. A potential field algorithm is then applied to drive the sailboat towards the goal while avoiding obstacles even when the goal is located directly downwind or upwind. Simulations, using a boat specific dynamic simulator, show that the proposed method can successfully drive an autonomous boat between a set of predefined waypoints under time varying wind conditions. This method is computationally efficient and is suitable for on-board real-time implementation.

I. INTRODUCTION

During the recent years, a growing activity concerning autonomous surface vehicles (ASV) has been noted. Applications for such vehicles include port protection [1], mines countermeasure [2], reconnaissance and surveillance mission [3]. Other vehicles for monitoring bathymetry data in shallow water [4] or various marine environments either alone [5]–[7] or as part of a sensor network [8]–[12] may also be cited. All of these aforementioned vehicles are conventional electric powered systems and suffer from a lack of autonomy that restrains their usage to short term missions. Sailboat robots could be an efficient solution for long term missions and semi-persistent presence in the oceans since they rely on renewable energy like solar and wind energy [13], [14]. However, steering such vehicles presents an inherent difficulty since the thrust force heavily rely on the wind (speed and direction) and sail angle as well as on the underlying complex dynamic properties of the ship, mainly due to the aero and hydrodynamic forces acting on the sail and on the hull.

In this paper, we present first the dynamic model of our sailboat prototype. This model takes into account both the aero and hydrodynamic forces acting on the ship as well as the inertial terms. A numerical and computationally efficient simulator is then derived from the set of differential

equations of motion, using experimental data recorded on a towing tank. Second, we propose a routing strategy for the computation of a suitable boat heading to reach a given waypoint. Since accurate weather forecasts are not available for short distances and periods, our algorithm takes into account only local and instantaneous wind conditions to compute an optimum heading for the vessel. The path planning algorithm will react to changes of the wind conditions as well as detected obstacles in real-time by recalculating the heading periodically, similarly to what a human sailor does on a short regatta. This method has been successfully tested under various wind conditions and have been validated in simulation using the aforementioned numerical simulator.

II. SAILBOAT MODELING

In this section the dynamic model of our prototype is presented. Both aero and hydrodynamic forces acting on the sailboat are taken into account to derive a realistic and computationally efficient numerical simulator.

A. Forces acting on the sails, keel and rudder

The forces acting on the sail can be expressed in terms of lift and drag components, both applied in a center of effort. The drag force F_D is in the direction of the apparent wind velocity and the lift force F_L is perpendicular to F_D . The magnitudes of these forces are related to the dimensionless lift coefficient C_l and drag coefficient C_d . C_l relates to the lift generated by the dynamic pressure of the wind flow around the sail; C_d quantify the resistance of the sail moving through the wind.

The lift and drag forces can be computed, in a sail reference frame, by the formulas of fluid mechanics (1).

$$\begin{cases} F_D &= \frac{1}{2} \rho S C_d v_f^2 \\ F_L &= \frac{1}{2} \rho S C_l v_f^2 \end{cases} \quad (1)$$

where ρ is the air density, S is the sail area and v_f is the apparent wind speed relative to the sail.

Since the rudder and the keel are airfoil-shaped bodies moving through a fluid, the hydrodynamic forces acting on these elements can also be computed using an expression similar to (1) and replacing ρ by water density, v_f by the relative water velocity and by using the specific lift and drag coefficients for rudder and keel.

B. Forces acting on the hull

The total hydrodynamic resistance R_{Hydro} acting on the hull can be written as (2):

$$R_{Hydro} = R_{Residuary} + R_{Friction} + R_{Leeway} + R_{Heel} \quad (2)$$

This work is supported by the ANR project ASAROME (Num. ANR-07-ROBO-0009)

M. A. Romero-Ramirez, C. Pêtrès and F. Plumet are with ISIR (Institut des Systèmes Intelligents et de Robotique) UPMC Univ Paris 06, CNRS - UMR 7222 4 place Jussieu, 75005 Paris - France lastname@isir.upmc.fr

B. Alessandrini is with Fluid Mechanics Laboratory, Ecole Centrale Nantes, CNRS - UMR 6598, 1 rue de la Noë, 44321 Nantes - France alessandrini@ec-nantes.fr

where $R_{Residuary}$ is the residuary resistance (mainly due to the waves created by the shape of the hull), $R_{Friction}$ the resistance induced by the fluid on the hull, R_{Leeway} the resistance induced by the leeway (angle between the boat main axis and the velocity vector) and R_{Heel} the heel (roll angle) induced resistance ([15], [16]).

Since the geometric parameters of the hull are compatibles with the valid interval of the Gerritsma's model [17] (see table I), $R_{Residuary}$ can be computed using the Gerritsma's equation (3). The coefficients a_0 to a_9 are given in [18] for a Froude number $F_N = v^2/gL_{WL}$ within the range from 0.125 to 0.450.

$$R_{Residuary} = mg \left[a_0 + a_1 \cdot C_P + a_2 \cdot LCB + a_3 \cdot \frac{B_{WL}}{T_C} + a_4 \frac{L_{WL}}{V^{1/3}} + a_5 \cdot C_P^2 + a_6 \cdot C_P \cdot \frac{L_{WL}}{V^{1/3}} + a_7 \cdot LCB^2 + a_8 \cdot \left(\frac{L_{WL}}{V^{1/3}} \right)^2 + a_9 \cdot \left(\frac{L_{WL}}{V^{1/3}} \right)^3 \right] \quad (3)$$

with:

C_P : prismatic coefficient,
 L_{WL} : length of the waterline (m),
 B_{WL} : width of the waterline (m)
 V : volume of the submerged part of the hull (m^3),
 LCB : longitudinal center of buoyancy corrective term,
 T_C : draught (m)

TABLE I
GERRITSMAS'S VALID VALUES INTERVAL

Coefficient	Min	Max	Measured Value
L_{WL}/B_{WL}	2.76	5	4.2
B_{WL}/T_C	2.46	19.32	3.0
$L_{WL}/V^{1/3}$	4.34	8.5	5.2
LCB	0	-6%	-2%
C_P	0.52	0.6	0.55

The other components $R_{Friction}$, R_{Leeway} and R_{Heel} of the hydrodynamic resistance of the hull are then experimentally identified using the towing tank (150m × 5m × 3m) of *Ecole Centrale de Nantes*. The hull, without keel and rudder, was mounted on a six DoF force-torque sensor with non restricted heave and sway (Fig. 1) and the resulting forces and torques have been recorded under various traction conditions, with and without heel and leeway. Longitudinal and lateral resistance forces are recorded for a range of velocities compatible with a Froude number $F_N \leq 0.45$. A sample of these data is shown in Fig. 2.

Based on the data recorded during the tests, a set of interpolated functions has been derived to model the total hydrodynamic resistance.

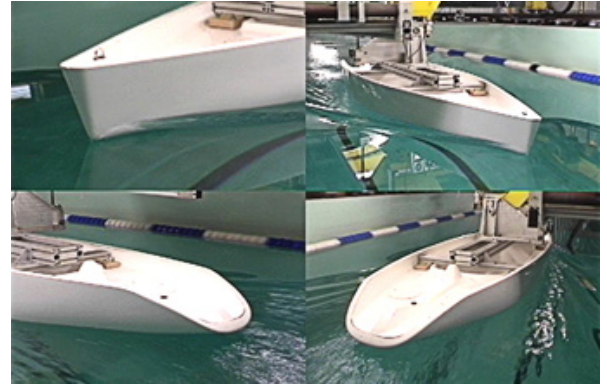


Fig. 1. Hull attached to a 6 components force-torque sensor in the ECN towing tank

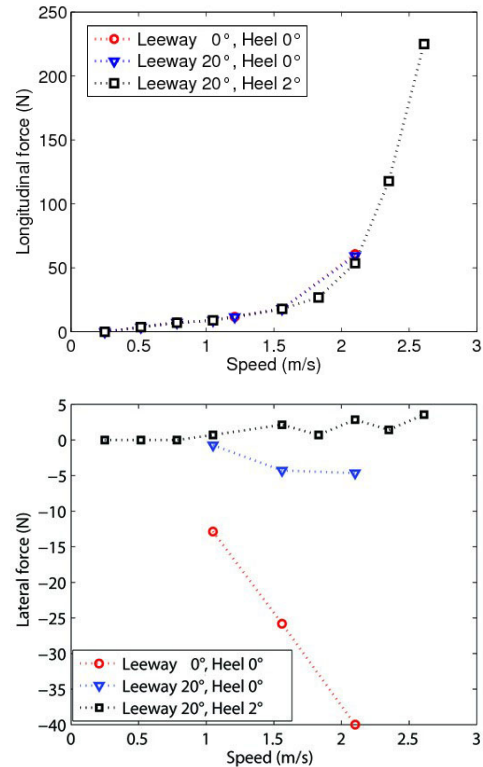


Fig. 2. Hydrodynamic longitudinal and lateral forces measured in the towing tank with and without leeway and heel

C. Motion Equation and Simulator

The sailboat motion equations can be written using the Newton-Euler's law in the reference frame R_B , as (4):

$$\begin{cases} m \left(\frac{d\vec{v}_{B/R_0}}{dt} \right)_{/R_B} = \vec{F}_{/R_B} - m(\vec{\Omega}_{R_B/R_0} \wedge \vec{v}_{B/R_0}) \\ \Pi_{B/G} \cdot \vec{\Omega}_{R_B/R_0} = \vec{M}_G - \vec{\Omega}_{R_B/R_0} \wedge \Pi_{B/G} \cdot \vec{\Omega}_{R_B/R_0} \end{cases} \quad (4)$$

$\vec{F}_{/R_B}$: total force acting on the sailboat.
 \vec{M}_G : total torque acting on the sailboat
 m : mass of the sailboat
 with: $\Pi_{B/G}$: inertial matrix of the sailboat
 \vec{v}_{B/R_0} : velocity vector of CoG in R_0
 $\vec{\Omega}_{R_B/R_0}$: angular velocity vector in R_0

R_0 is an Earth-fixed inertial frame and R_B is a Body-fixed reference frame, with its origin at the ship's center of gravity (CoG).

From this analytical description of the dynamics of our sailboat, a numerical simulator has been built, which integrates the differential equations of motion using a classical Runge-Kunta algorithm. This numerical simulator can then be used to simulate the behaviour of our prototype under different environmental conditions (see section IV-B).

The numerical model can also be used to compute the speed polar diagram of the sailboat (see Fig. 3). These performance curves correspond to the steady-state maximum velocity of the vehicle for a given wind speed and a given wind direction and for headings φ relative to the wind direction varying from 45° to 315° . To keep a constant heading with respect to the wind until the simulation reaches the steady-state for the vehicle velocity, a PID controller on the rudder and on the boom has been used.

For wind speeds relative to the ground (TWS for true wind speed) varying from 5 to 20 knots, speed profiles look similar. A so-called *upwind no-go zone* is discarded for $-45^\circ \leq \varphi \leq 45^\circ$. Another critical sailing zone, called *downwind no-go zone*, is exhibited for $150^\circ \leq \varphi \leq 210^\circ$. In fact the boat is able to navigate in this region, but for safety reasons (instability) these headings will also be avoided in practice. The performance curves will also be used to trim the sail angle in real-time to reach a given reference in terms of vehicle velocity and heading for given wind speed and direction. The description of this sail trimming algorithm is out of the scope of this article.

A high potential will be affected to these upwind and downwind sailing regions in the path planner presented in the next section.

III. PATH PLANNING

In the recent years, numerous methods have been proposed for the path planning of autonomous sailboats : based on logic rules [19], [20], state machine [21]–[23], neural control [24] or ray-tracing techniques [25]. Potential fields methods, due to Khatib [26] and Krogh [27], have been successfully employed for robot control and motion planning of mobile robots (see for example [28]–[31] among many others).

The originality of our method is to adapt this popular potential field approach to reactive path planning of a sailboat by building a so-called local potential around the boat location to take upwind and downwind sailing constraints into account. An hysteresis potential relative to the cost of tacking (turning the bow through the wind) and gybing (turning the stern through the wind) is also proposed, which

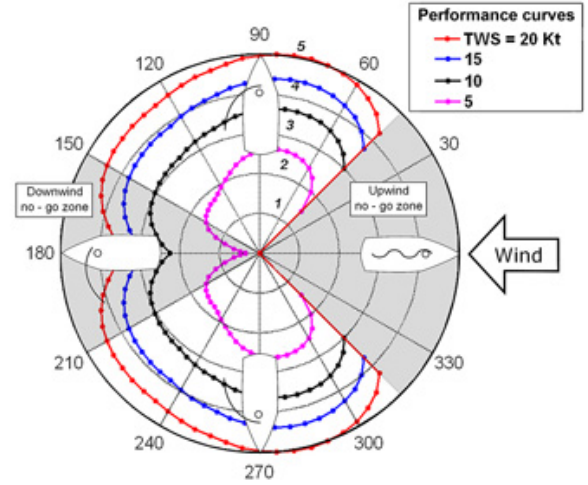


Fig. 3. Speed polar diagram of our sailboat computed for four different wind speeds. The upwind and downwind no-go zones are depicted in gray on this figure

makes our method easy to tune according to the vehicle specifications.

The main drawback with potential field techniques is their susceptibility to local minima possibly exhibited by non-convex objects. In our case, this problem is not an issue for two reasons. First, detected obstacles are substituted for their own convex hull. For instance, a crescent-shaped island will be represented as an ellipse. Second, the set of waypoints the boat has to reach, while reactively avoiding obstacles, is supposed to be chosen away from the coasts in order to stay in convex navigation regions.

Our potential field approach is decomposed in two parts, a global potential field and a local potential field. The global potential field is relative to the goal point and to the obstacles. The local potential field is relative to the wind direction.

A. Global potential

The global potential is computed in order to attract the vehicle towards the goal point and to move it away from the obstacles.

a) *Potential relative to the goal point*: In order to attract the vehicle towards the goal point, a linear potential P_g is built for every point P of the map as follows:

$$P_g = G_g \cdot \text{dist}(P, P_{goal})$$

where G_g is the desired attractive gradient and $\text{dist}(P, P_{goal})$ is the Euclidean distance between P and the goal point P_{goal} . Since G_g is a constant, the potential P_g looks like a cone centered on P_{goal} (see Fig. 4).

b) *Potential relative to the obstacles*: A repulsive potential P_o relative to the obstacles located in P_{obst} is built for every point P of the map as follows:

$$P_o = \frac{k}{\text{dist}(P, P_{obst})}$$

where k is a tunable scalar. This potential tends to infinite as we come close to the obstacles. The position of each

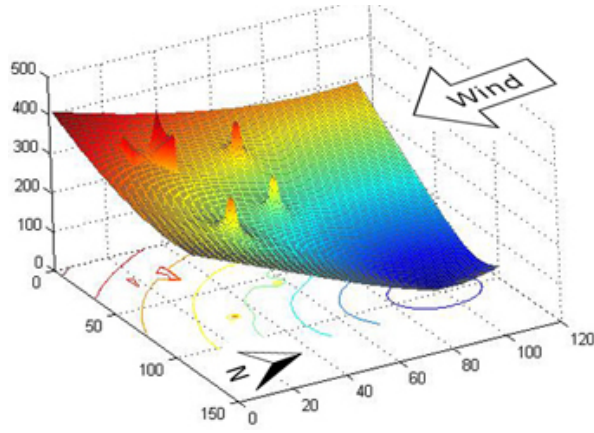


Fig. 4. Illustration of the overall potential relative to three obstacles and to a goal point located at the North-East corner of the map

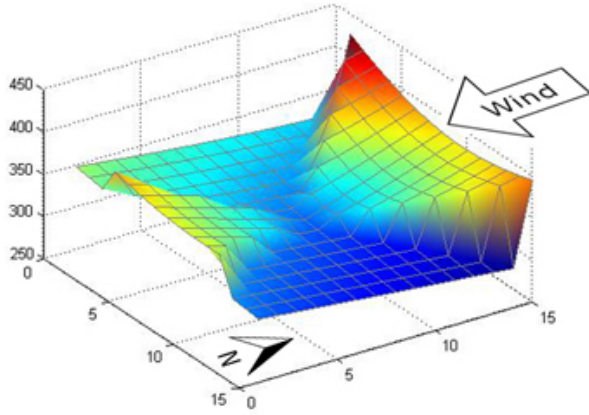


Fig. 5. Close-up on the local potential around the boat. In this case the upwind no-go zone is pointing up because the wind is coming from North

obstacles can be known in advance or can be updated in real time by on board navigation sensors.

B. Local potential

The local potential is built in the neighborhood of the boat location. It is rebuilt after each displacement of the boat according to the wind direction and the latest tack (see Fig. 5).

a) *Upwind potential*: In order to take the upwind no-go zone into account a so-called upwind potential P_{up} is built dynamically for each point P_w inside a window centered on the boat location P . The magnitude of P_{up} is a function of the angle ϕ between the direction of \vec{PP}_w and the wind direction TWA . It is linear inside the upwind no-go zone sector (defined by the angle ϕ_{up} , see Fig. 6) and null outside:

$$\begin{cases} P_{up} = G_{up} \cdot \text{dist}(P_w, P) & \text{if } 0 < |\phi| < \phi_{up} \\ P_{up} = 0 & \text{elsewhere} \end{cases}$$

where G_{up} is the desired gradient inside the upwind no-go zone sector.

b) *Downwind potential*: To take into account the downwind no-go zone, a so-called downwind potential P_{down} is

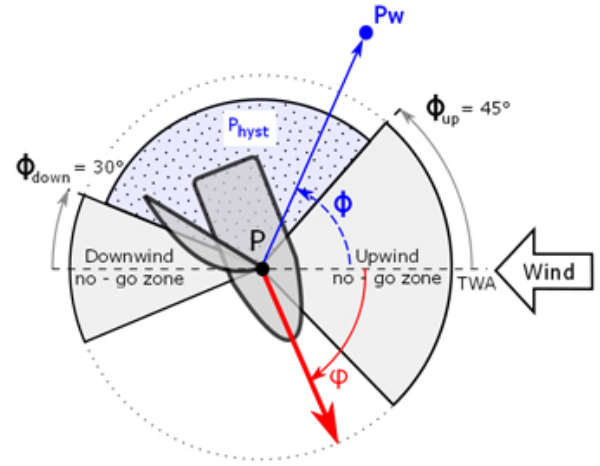


Fig. 6. Scheme of the upwind and downwind no-go zones. The dotted region corresponds to the region where $P_h \neq 0$

defined in the same way as the upwind potential, except for the angle ϕ_{down} , which defines the downwind no-go zone sector (see Fig. 6):

$$\begin{cases} P_{down} = G_{down} \cdot \text{dist}(P_w, P) & \text{if } 0 < |\phi - \pi| < \phi_{down} \\ P_{down} = 0 & \text{elsewhere} \end{cases}$$

where G_{down} is the desired gradient inside the downwind no-go zone sector.

c) *Gybe and tack potential*: In order to take the cost of gybing and tacking into account a so-called hysteresis potential P_h is built dynamically for each point P_w inside the window centered on the boat location P . The magnitude of P_h is a function of the angle ϕ and the latest tack. For instance, if the boat navigates with the wind coming from its left side, P_h will be defined at the right side of the wind direction to prevent the boat to tack or gybe too frequently (see Fig. 6). In this example P_h is defined as follows:

$$\begin{cases} P_h = G_h \cdot \text{dist}(P_w, P) & \text{if } \phi_{up} < \phi < \pi - \phi_{down} \\ P_h = 0 & \text{elsewhere} \end{cases}$$

where G_h is the desired gradient of P_h . This way, only one parameter has to be set up to fit the cost of gybing and tacking.

C. Gradient descent

Once the local potential has been built and added to the global potential, a gradient descent is carried out on the overall potential $P_t = P_g + P_o + P_{up} + P_{down} + P_h$ to find the new heading for the boat. Practically, a profile of the potential P_t around the boat location P is extracted along a ring centered in P with a radius R defined as a function of the window size W_{size} , $R = W_{size} - 1$. The heading ϕ for the next move is the angle corresponding to the global minimum of the profile. The gradient descent algorithm is stopped when the boat arrives in the vicinity of the goal point. Precisely, the stop criteria is defined as follows: $\text{dist}(P, P_{goal}) < \epsilon$, with $\epsilon = W_{size}$.

IV. RESULTS

For the sake of clarity, the environment in the following simulations is assumed to be static (obstacles are fixed) and completely known (obstacles are mapped without uncertainty). Besides, the wind is assumed to be constant in direction as well as in velocity. However, since our local potential is incrementally built as a function of instantaneous wind conditions and visible obstacles around the boat location, this reactive path planning approach holds for dynamic environments and can be implemented without any change on real embedded systems.

In the following simulations, default parameters for the potential have been set up as follows: $G_g = 3$, $k = 100$, $G_{up} = 10$, $G_{down} = 5$, $G_h = 2$, $\phi_{up} = 45^\circ$, $\phi_{down} = 30^\circ$.

A. Upwind navigation example

This example describes a sensitive manoeuvre for a sailboat: beating to windward. Fig. 7 depicts trajectory solutions exhibited by the potential field based path planner for a wind coming from North-East. Several hysteresis potentials have been tested. The red trajectory has been computed with $G_h = 3$, the blue trajectory has been computed with $G_h = 2$ and the black trajectory has been computed with $G_h = 1$. Distance and travel time of these trajectories are similar but two, three and seven tacks have been respectively executed to reach the goal point.

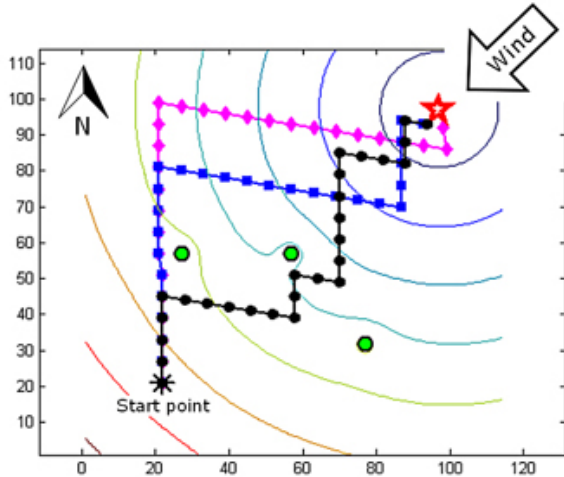


Fig. 7. Trajectories computed with the wind coming from North-East using different hysteresis potentials. In red $G_h = 3$, in blue $G_h = 2$, in black $G_h = 1$

As we can see, the proposed path planner provides coherent trajectories in terms of heading constraints for a sailboat. Trajectories follow admissible headings regarding the upwind no-go zone (similar results are obtain for downwind navigation). The number of gybes and tacks may be tuned by the hysteresis potential to suit the real cost of these manoeuvres. Besides, attractiveness of the goal point and repulsiveness of obstacles are easily tunable in this potential field framework.

B. Numerical path planning validation

In this section, realism of the solutions given by the path planing algorithm is improved by using the dynamic model of the sailboat described in section II.

In the simulations so far the vehicle dynamics has been neglected. Resulting paths extracted from the start to the goal point may not be physically admissible for a given sailboat. Introducing the sailboat dynamics would greatly improve the reliability of the overall path planning method. At each step of the path planning algorithm, the numerical simulator is run and the resulting position and heading of the sailboat will be used as the current state for the next step.

In the following example, the boat initial velocity is equal to zero and the boat is pointing towards the goal point. The low level control loop for the boom angle and for the rudder angle is a simple PID controller that makes the heading converging to the heading reference given by the high level path planner.

A comparison between a trajectory computed using only the high level path planner and a trajectory resulting from the coupling of the path planner with the numerical simulator is given in Fig. 8. In this framework, where the wind comes from East, the boat begins to accelerate in the direction given by the path planner. At this stage of the simulation both trajectories are similar in terms of heading. To reach the target a gybe is theoretically necessary at some point of the trajectory, as depicted by the black curve. While easily done when neglecting the vehicle dynamics, this manoeuvre is far from immediate in practice. The inertia of the boat may impact such a turn in the trajectory, as depicted by the blue curve.

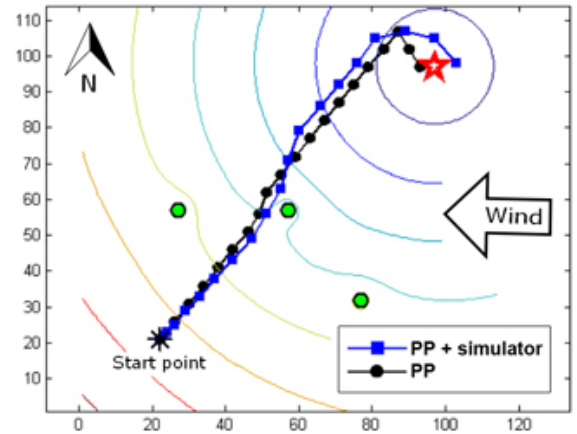


Fig. 8. Trajectories computed with the high level path planner only (PP) and by coupling the high level path planner and the low level simulator (PP + simulator)

V. CONCLUSION AND FUTURE WORKS

In this work, a reactive path planning method for the navigation of an autonomous sailboat has been presented. This path planning algorithm, based on the potential field

approach, reacts to changing wind conditions as well as detected obstacles in real-time by recalculating the heading periodically. This method have been successfully tested and validated in simulation under various wind conditions, using a computational efficient numerical simulator specifically tuned for the boat that will be used in the next future.

This 3.6 m long sailboat based on a mini-J hull (a reduced scale of a 12M JI class) is currently under development (see Fig. 9). The electrical power is provided by a battery pack, charged by a wind turbine and a 0.5m² solar panel. She will use on-board navigation sensors (IMU, GPS, anemometer and wind vane) as well as perception sensors (sonar, hydrophones and panoramic camera) for obstacles detection.



Fig. 9. A view of the first field test trial of the sailboat on the river Erdre near Nantes in France

REFERENCES

- [1] J. Manley, "Unmanned surface vehicles, 15 years of development," in *MTS/IEEE OCEANS 2008*, 2008.
- [2] M. Robin, S. Eric, G. Chandler, C. Charlie, H. Mike, and P. Kevin, "Cooperative use of unmanned sea surface and micro aerial vehicles at hurricane wilma," *Journal of Field Robotics*, vol. 25, no. 3, pp. 164–180, 2008.
- [3] T. Pastore and V. Djapic, "Improving autonomy and control of autonomous surface vehicles in port protection and mine countermeasure scenarios," *Journal of Field Robotics*, vol. 27, no. 6, pp. 903–914, 2010.
- [4] P. Mahacek, T. Berk, A. Casanova, C. Kitts, W. Kirkwood, and G. Wheat, "Development and initial testing of a swath boat for shallow-water bathymetry," in *MTS/IEEE OCEANS 2008*, 2008.
- [5] E. Steimle and M. Hall, "Unmanned surface vehicles as environmental monitoring and assessment tools," in *MTS/IEEE OCEANS 2006*, 2006.
- [6] P. Mahacek, R. Kobashigawa, A. Schooley, and C. Kitts, "The wasp: an autonomous surface vessel for the university of alaska," in *MTS/IEEE OCEANS 2005*, 2005, pp. 2282 – 2291 Vol. 3.
- [7] M. Caccia, R. Bono, G. Bruzzone, E. Spirandelli, G. Veruggio, A. Stortini, and G. Capodaglio, "Sampling sea surfaces with sesamo: an autonomous craft for the study of sea-air interactions," *IEEE Robotics Automation Magazine*, vol. 12, no. 3, pp. 95 – 105, 2005.
- [8] A. Pascoal, P. Oliveira, C. Silvestre, and et al, "Robotic ocean vehicles for marine science applications: the european asimov project," in *MTS/IEEE OCEANS 2000*, 2000, pp. 409–415 vol.1.
- [9] A. Dhariwal and G. Sukhatme, "Experiments in robotic boat localization," in *IEEE/RSJ Int. Conf. on Intelligent Robots and Systems*, 2007, pp. 1702 –1708.
- [10] G. Podnar, J. Dolan, A. Elfes, S. Stancliff, E. Lin, J. Hosier, T. Ames, J. Moisan, T. Moisan, J. Higinbotham, and E. Kulczycki, "Operation of robotic science boats using the telesupervised adaptive ocean sensor fleet system," in *IEEE Int. Conf. on Robotics and Automation*, 2008, pp. 1061 –1068.
- [11] J. Curcio, J. Leonard, and A. Patrikalakis, "Scout - a low cost autonomous surface platform for research in cooperative autonomy," in *MTS/IEEE OCEANS 2005*, 2005, pp. 725 – 729 Vol. 1.
- [12] D. Eickstedt, M. Benjamin, H. Schmidt, and J. Leonard, "Adaptive control of heterogeneous marine sensor platforms in an autonomous sensor network," in *IEEE/RSJ Int. Conf. on Intelligent Robots and Systems*, 2006, pp. 5514 –5521.
- [13] N. Cruz and J. Alves, "Autonomous sailboats: An emerging technology for ocean sampling and surveillance," in *MTS/IEEE OCEANS 2008*, 2008.
- [14] P. Rynne and K. von Ellenrieder, "A wind and solar-powered autonomous surface vehicle for sea surface measurements," in *OCEANS 2008*, 2008.
- [15] D. Harris, G. Thomas, and M. Renilson, "Downwind performance of yachts in waves," in *2nd Australian Sailing Science Conference*, 1999.
- [16] E. Jacquin, Y. Roux, P.-E. Guillermin, and B. Alessandrini, "Toward numerical vpp with the full coupling of hydrodynamic and aerodynamic solvers for acc yacht," in *17 Chesapeake Sailing Yatch Symposium*, 2005.
- [17] J. Gerritsma, J. Keuning, and R. Onnink, "Results and analysis of the delft systematic series ii yacht hull form experiments," in *11th HISWA Int. Symp. on Yacht Design and Yacht Construction*, 1990.
- [18] J. Gerritsma, J. Keuning, and R. Onnik, "Sailing yacht performance in calm water and in waves," in *12th International Symposium on Yacht Design and Construction*, HISWA., 1992.
- [19] M. Neal, "A hardware proof of concept of a sailing robot for ocean observation," *IEEE Journal of Oceanic Engineering*, vol. 31, no. 2, 2006.
- [20] R. Stelzer and T. Proll, "Autonomous sailboat navigation for short course racing," *Robotics and Autonomous Systems*, vol. 56, no. 7, pp. 604 – 614, 2008.
- [21] Y. Briere, F. L. Cardoso Ribeiro, and M. Vieira Rosa, "Design methodologies for the control of an unmanned sailing robot," in *8th Conf. on Manoeuvring and Control of Marine Craft*, 2009.
- [22] G. Elkaim and C. Boyce, "Energy scavenging and aerodynamic performance of a rigid wing propulsion system for an autonomous surface vessel," in *ION Global Navigation Satellite Systems Conference*, 2009.
- [23] H. Erckens, G.-A. Busser, C. Pradalier, and R. Siegwart, "Avalon: Navigation strategy and trajectory following controller for an autonomous sailing vessel," *IEEE Robotics Automation Magazine*, vol. 17, no. 1, pp. 45 –54, 2010.
- [24] C. Sauze and M. Neal, "A neuro-endocrine inspired approach to long term energy autonomy in sailing robots," in *Proc. TAROS 2010 : Towards Autonomous Robotic Systems*, 2010.
- [25] R. Stelzer, K. Jafarmadar, H. Hassler, and R. Charwot, "A reactive approach to obstacle avoidance in autonomous sailing," in *3rd Int. Robotic Sailing Conference*, 2010.
- [26] O. Khatib, "Real-time obstacle avoidance for manipulators and mobile robots," *International Journal of Robotics Research*, vol. 5, no. 1, pp. 90–98, 1986.
- [27] B. Krogh and C. Thorpe, "Integrated path planning and dynamic steering control for autonomous vehicles," in *IEEE Int. Conf. on Robotics and Automation*, vol. 3, 1986, pp. 1664–1669.
- [28] J. Barraquand, B. Langlois, and J.-C. Latombe, "Numerical potential field techniques for robot path planning," *IEEE Transactions on Systems, Man and Cybernetics*, vol. 22, no. 2, pp. 224 –241, 1992.
- [29] H. Haddad, M. Khatib, S. Lacroix, and R. Chatila, "Reactive navigation in outdoor environments using potential fields," in *IEEE Int. Conf. on Robotics and Automation*, vol. 2, 1998, pp. 1232 –1237.
- [30] S. Ge and Y. Cui, "Dynamic motion planning for mobile robots using potential field method," *Autonomous Robots*, vol. 13, no. 3, pp. 207 –222, 2002.
- [31] S. Shimoda, Y. Kuroda, and K. Iagnemma, "Potential field navigation of high speed unmanned ground vehicles on uneven terrain," in *IEEE Int. Conf. on Robotics and Automation*, 2005, pp. 2828 – 2833.